Early changes of pulmonary arterial hemodynamics in patients with systemic sclerosis: Flow pattern, WSS and OSI analysis with 4D Flow MRI

Early changes of pulmonary arterial hemodynamics in patients with systemic sclerosis: Flow pattern, WSS and OSI analysis with 4D Flow MRI

Takenori Ikoma[1]*, MD, Kenichiro Suwa[1]*§, MD PhD, Makoto Sano[1], MD PhD, Takasuke Ushio[2], MD, Masao Saotome[1], MD PhD, Noriyoshi Ogawa[3], MD PhD, Hiroshi Satoh[4], MD PhD, Yuichiro Maekawa[1], MD PhD

* Takenori Ikoma and Kenichiro Suwa contributed equally to this work.

[1]Division of Cardiology, Internal Medicine 3, Hamamatsu University School of Medicine, 1-20-1 Handayama, Higashi-ku, Hamamatsu, 431-3125, Japan.

[2]Department of Diagnostic Radiology, Hamamatsu University School of Medicine, 1-20-1 Handayama, Higashi-ku, Hamamatsu, 431-3125, Japan.

[3]Division of Rheumatology, Internal Medicine 3, Hamamatsu University School of Medicine, 1-20-1 Handayama, Higashi-ku, Hamamatsu, 431-3125, Japan.

[4]Department of Cardiology, Fujinomiya City General Hospital, 3-1 Nishiki-cho, Fujinomiya, 481-0076, Japan.

§ Address for Correspondence: Kenichiro Suwa, MD PhD.

Division of Cardiology, Internal Medicine 3, Hamamatsu University School of Medicine, 1-20-1 Handayama, Higashi-ku, Hamamatsu, 431-3192, Japan.

Fax: +81-53-435-2742, Tel: +81-53-435-2267, E-mail address: k-suwa@hama-med.ac.jp

Early changes of pulmonary arterial hemodynamics in patients with systemic sclerosis: Flow pattern, WSS and OSI analysis with 4D Flow MRI

Abstract

Objectives- To study the pulmonary artery (PA) hemodynamics in patients with systemic sclerosis (SSc) using 4D flow MRI (4D-Flow).

Methods - Twenty-three patients with SSc (M/F: 2/21, 57±15 years, 3 manifest PA hypertension (PAH) by right heart catheterization) and 10 control subjects (M/F: 1/9, 55±17 years) underwent 4D-Flow for the in vivo measurement of 3D blood flow velocities in the PA. Data analysis included area-averaged flow quantification at the main PA, 3D wall shear stress (WSS), oscillatory shear index (OSI) calculation along the PA surface and Reynolds number. The composite outcome of all-cause death and major adverse cardiac events was also investigated.

Results- The maximum PA flow at the systole didn't differ, but the minimum flow at the diastole was significantly greater in patients with SSc compared to that in control subjects (7.7±16.0 ml/s vs. -13.0±17.3 ml/s, $p<0.01$). The maximum WSS at the peak systole was significantly lower and OSI was significantly greater in patients with SSc compared to those in control subjects (maximum WSS: 1.04±0.20 Pa vs. 1.33±0.34 Pa, $p<0.01$, OSI: 0.139±0.031

vs. 0.101±0.037, p<0.01). The cumulative event-free rate for the composite event were significantly lower in patients with minimum flow in main PA ≤9.22 ml/s (p=0.012) and in patients with Reynolds number ≤2560 (p<0.001).

Conclusions- 4D-Flow has the potential to detect changes of PA hemodynamics noninvasively and predict the outcome in patients with SSc at the stage before manifest PAH.

Key words

Magnetic resonance imaging; pulmonary artery; hemodynamics; blood flow velocity; systemic sclerosis.

Key points

- The WSS at the peak systolic phase was significantly lower (p<0.05), whereas OSI were greater (p<0.01) in patients with SSc without manifest PAH than controls.
- The hemodynamic change detected by 4D-Flow may help patient management even at the stage before manifest PAH in SSc.
- The minimum PA flow and Reynolds number by 4D-Flow will serve as a predictive marker for SSc.

Abbreviations

CTL; control subjects, EAE; effective arterial elastance, EDV; end-diastolic volume, FA;

flip angle, FIESTA; fast imaging employing steady state acquisition, FOV; field of view, FSPGR; fast spoiled gradient echo, IR-FGRE; inversion recovery prepared fast gradient echo, LGE; late gadolinium enhancement, LV; left ventricular, MACE; major adverse cardiac events, MRI; magnetic resonance imaging, NEX; number of excitations, NT-proBNP; N-terminal-pro brain natriuretic peptide, OSI; oscillatory shear index, PA; pulmonary artery, PAH; pulmonary arterial hypertension, RV; right ventricular, RVSP; peak right ventricular systolic pressure, pSSc; patient with systemic sclerosis, RBW; receiver band width, Re; Reynolds number, ROC; receiver-operating characteristic, SD; standard deviation, SSc; systemic sclerosis, SV; stroke volume, TR; repetition time, TRPG; tricuspid regurgitation pressure gradient, TTE; transthoracic echocardiography, VENC; velocity encoding, WSS; wall shear stress, 3D; Three-dimensional, 3DFT; three dimensional Fourier transform, 4D-Flow; Three-dimensional cine phase contrast MR imaging

Introduction

Cardiovascular involvement in systemic sclerosis (SSc) is heterogeneous, including the myocardium, pericardium, and coronary, renal, and pulmonary circulations [1, 2]. Although the prevalence of pulmonary arterial hypertension (PAH) in SSc is 7.8% - 12%, SSc accounts for a large proportion in connective tissue disease-associated PAH and has prognostic significance [3-5].

The examination of pulmonary arterial (PA) hemodynamics is crucial to identify patients who are most likely to benefit from earlier therapy. However, the high prevalence of both left heart disease and interstitial lung disease makes the PA hemodynamics in pSSc more complex. Conventional heart examinations including transthoracic echocardiography (TTE) have been used as non-invasive screening tests [6-9]. However, these indices lack specificity and fail in an exact estimation of altered PA hemodynamics.

Alterations in flow features and wall shear stress (WSS) in PA have been known to associate with vessel remodeling and PAH [10-12]. Three-dimensional (3D) cine phase contrast MR imaging (4D-Flow) has attracted great interest and is a reliable tool for analyzing characteristic flow features in the great vessels and heart [13-15]. Recently, 4D-Flow was used to visualize the flow vectors in PA, and both helical flow and reduced WSS were reported in patients with PAH [16].

We hypothesized that both PA flow features and WSS would be changed in pSSc, even in the stage before manifest PAH. To clarify the changes of PA hemodynamics, 4D-Flow images were analyzed for streamline and WSS in pSSc and control subjects (CTL). We also investigated the outcome of pSSc to predict the adverse event using 4D-Flow.

Materials and Methods

Patients

Fifty-five consecutive pSSc attending the rheumatology clinic at Hamamatsu University Hospital between January 2012 and May 2015 were prospectively selected. The diagnosis of SSc was based on the guideline of the Japanese Ministry of Health and Welfare [17]. Seven pSSc were excluded because of coronary arterial disease, severe valve disease, renal insufficiency (estimated glomerular filtration rate <30 ml/min/1.73 m^2), implanted pacemaker, or no informed consent. The remaining 48 pSSc underwent cardiac MR imaging (MRI) for the screening of cardiac involvement. Three pSSc with arrhythmia and 22 who did not undergo TTE within one month before MRI were excluded from the study. Finally, remained 23 patients were selected for 4D-Flow. Cardiac MRI with 4D-Flow was also examined in sex- and age-matched 10 healthy subjects without any organic heart diseases or any conventional risk factors for cardiovascular diseases as CTL. This study protocol was conducted in accordance with the Declaration of Helsinki and was approved by an institutional review board. All study participants provided informed consent.

Serological tests, 12-lead electrocardiogram (ECG), and TTE

All pSSc and CTL underwent ECG, and TTE (iE33; Phillips Medical Systems, Andover,

USA) within one month. Serological tests including N-terminal-pro brain natriuretic peptide (NT-proBNP) and autoimmune antibodies (anti-Scl-70, anti-centromere, and anti-U1-RNP antibodies) were also examined in pSSc. In TTE, each chamber size, left/right ventricular (LV/RV) wall motion, curvature of the interventricular septum, and pericardial effusions were evaluated. The peak velocity of the tricuspid regurgitation jet was measured, and the pressure gradient (TRPG) was calculated with the simplified Bernoulli's equation [6]. The peak RV systolic pressure (RVSP) was determined by adding estimated right atrial pressure to TRPG [18].

MRI

All MRI examinations were performed using a 3T MR scanner (Discovery MR750, GE Healthcare, Waukesha, USA) with maximum gradient strength of 50 mT/m and a maximum slew rate of 200 mT/m/ms with a commercially available 12-channel phased array body coil. Typically, 2D-fast imaging employing steady state acquisition (FIESTA) and late gadolinium enhancement (LGE) images were acquired in the short axis, vertical and horizontal long axis orientations. The slice thickness/gap was typically 10 mm/0 mm (6-9 slices). 2D-FIESTA cine images were based on the steady state free precession sequence, and LGE imaging was on the inversion recovery prepared fast gradient echo (IR-FGRE) sequence.

Contrast-enhanced 3D FSPGR MR angiography was performed for geometric information

of 4D-flow as well as PA area quantification with TR (ms)/TE (ms)/FA (degrees)/NEX of 2.7/1.0/12/1, FOV (cm) 32, matrix reconstructed matrix with the aid of zero fill interpolation 224 × 224, RBW 83.3 kHz, and imaging time of 33 s for 4 phases. Bolus injection of 0.1 mmol/kg gadolinium chelate Gd-DTPA-BMA or Gd-DTPA (Daiichi Pharma Co. or Bayer Healthcare, Tokyo**,** Japan) was performed at an injection rate of 2.0 ml/s, followed by 20 ml of saline. 4D-Flow provides time-resolved 3D voxel data, each of which has 3D flow velocity components [19]. Imaging parameters used for coronal 3D Fourier transform (3DFT) fast spoiled gradient echo (FSPGR)-based 4D-Flow were as follows: repetition time (TR; ms)/echo time (TE; ms)/flip angle (FA; degrees)/number of excitations (NEX) of 4.5-5.0/2.0/15/1, field of view (FOV) 32 cm, matrix 224 × 224, 2-mm thickness, 60 partitions, 20 phases during one cardiac cycle, velocity encoding (VENC) 200 cm/s, and receiver band width (RBW) 83.3 kHz. The temporal resolution was 48-69 ms. Respiratory-compensated retrospective cardiac gating was performed. The resultant approximate imaging time was 10 min with a reduction factor of 2 for an auto-calibrating reconstruction for Cartesian sampling [20]. Raw data of 4D-Flow were transferred to a personal computer (Intel Xeon E3-1270 [3.4 GHz/Quad-core] DDR3, 16 GB ECC, Linux) and reconstructed.

Conventional cardiac MRI parameters

LV end-diastolic volume (LVEDV), LVEF, stroke volume (SV), RVEDV, RVEF, PA area

just above the pulmonary valve at the end-diastolic phase, and the prevalence of LGE were measured using a software (Cardiac VX, GE Healthcare, Waukesha, USA). LVEDV, RVEDV, SV, and PA area were indexed by dividing by body surface area (BSA) calculated by Du Bois formula. The effective arterial elastance (EAE) as an index of RV afterload was calculated by dividing TTE-derived RVSP by SV [21].

Post-processing for 4D-Flow

4D-Flow and MR angiographic data sets were formatted by DICOM and analyzed in a personal computer (Intel Core i7 CPU, 3.2 GHz, 12 GB RAM, Microsoft Windows 7). Segmentation, visualization of flow pattern, and calculation of WSS were performed by Flova (R'-Tech Co., Hamamatsu, Japan). The regions of interest including the main, right, and left PAs were determined from the 4D-Flow and MR angiographic data set. Segmentation was performed for vascular wall structures from 3D data sets of MR angiography at the peak of R wave with magnitude images (Gd-enhanced MRA image) of 4D-Flow using the region growing method. Their shapes were created by the marching cubes method.

The 3D flow information was interpolated with a spatial resolution of $2 \times 2 \times 2$ mm^3 using the 3D data sets. Three emitter planes traversing the bases of main, right, and left PAs were manually set, subsequently generating 3D streamline images with the Runge–Kutta method. The 3D streamlines are integrated traces along the instantaneous velocity vector field that are

color-coded according to the local velocity magnitude.

PA flow was evaluated based on the 3D streamline in each time frame. PA flow patterns were divided into: 1) non-helical (no rotational flow or flow rotation <360° at any PA segment and time frame); 2) focally helical (flow rotation ≥360° at one PA segment in some frames); and 3) diffusely helical (flow rotation ≥360° at two or more PA segments in some frames) in a blinded fashion by two independent observers. The plane traversing the base of main PA was then set, and the PA flow volume curve was obtained by multiplying the mean flow velocity with the PA area using Flova. The Reynolds number (Re) was calculated in each patient by the equation: $Re=\rho VL/\mu$, where ρ: density=1.05 g/cm^3, μ: viscosity=4.0×10^{-3} Pa×s, and V and L: area-averaged peak velocity and vessel diameter at the base of main PA. RV-PA coupling parameters of PA acceleration time, PA pulsatility index, and RVSV/RVESV were calculated. The equation for PA pulsatility index was as follows: (peak systolic velocity – minimum diastolic velocity) / (mean velocity).

Both the WSS and oscillatory shear index (OSI) distribution maps in the PAs were color-coded and visualized as 3D images. Temporal changes in the entire surface area-averaged WSS at PA wall during one cardiac cycle were described, and maximum and minimum WSS and OSI were estimated using Flova (Appendix and supplementary Figure 1). The overall post-processing time was approximately 60 min.

Outcome measures

The primary outcome was the all-cause death. The secondary outcomes included major adverse cardiac events (MACE), new onset of PAH, SSc-related hospitalization. Finally, composite outcome of all-cause death and MACE were evaluated.

Statistical analysis

Continuous data are expressed as means±standard deviation (SD) or as medians with interquartile range, as appropriate. Categorical data are shown as numbers and percentages. Continuous variables were compared by the two-sided unpaired *t*-test or Mann-Whitney U-test. Categorical variables were compared by Fisher's exact test. The inter-observer variability for the determination of helical flow patterns was evaluated by calculating Cohen's kappa (κ) coefficient. Correlations were assessed by Pearson's correlation coefficient (r) and linear regression analysis. The receiver-operating characteristic (ROC) analysis were performed for the evaluation of diagnostic accuracy. The cut-off value was decided by Youden Index. Kaplan-Meier method with the log-rank test were used for the outcome test. Values of $p<0.05$ were considered significant. All statistical analyses were performed using a statistical software package (SPSS 18.0; SPSS Inc., Chicago, USA).

Results

Patient characteristics

Age and gender of pSSc were 57.4±14.9 years and 91.3% female; three had manifest PAH confirmed by right heart catheterization (Table 1). Serum NT-proBNP levels were generally less than 400 pg/ml, but two pSSc with manifest PAH had high values (655 and 1052 pg/ml). Medications were mainly corticosteroids, immunosuppressants, and prostanoids. Sildenafil and/or ambrisentan were used for two pSSc with manifest PAH. Anti-Scl-70, anti-centromere, and anti-U1-RNP antibody were positive in three (13.0%), five (21.7%) and seven (30.4%) pSSc, respectively.

Abnormalities on ECG and TTE were shown in Supplementary Table 1. One patient with manifest PAH (SSc #23, Supplementary Table 1) showed signs of RV dilatation. Tricuspid regurgitation was observed in 15 pSSc, and RVSP exceeded 40 mmHg in three pSSc with manifest PAH (SSc #21-#23, Supplementary Table 1). No patients demonstrated pulmonary valve stenosis. On cine- and LGE-MRI, one patient exhibited low LVEF and five patients presented with LGE in the LV myocardium. No pSSc had LGE at the RV or atrial wall. EAE was higher in pSSc with manifest PAH than those without manifest PAH (1.07±0.90 mmHg/ml vs. 0.49±0.11 mmHg/ml, $p<0.05$).

CTL were 90% female and aged 54.5±17.3 years (p=ns. vs. pSSc). No CTL exhibited

abnormalities on ECG, TTE, and MRI.

PA Flow patterns analyzed with streamline imaging

Figure 1 shows representative streamline images of PA flow at peak and late systolic and early diastolic phases (supplementary movies 1-4). The right panels are area-averaged PA flows during one cardiac cycle.

The PA flow remained non-helical at any phase in five CTL, while in the other five, the focal helical flow was observed and localized at the main PA (Supplementary Table 1). Thirteen pSSc presented with diffusely helical flow, six exhibited focally helical flow, and only four had remaining non-helical flow. The helical flow developed mostly in the posterior wall of main PA, and there was a trend of high prevalence in the right PA (right: 52% vs. left: 35%). The helical flow continued from the late systolic phase to the early diastolic phase with a range of 92-651 ms (median 273 ms). Duration of helical flow was significantly longer in the subjects with diffuse helical flow compared to those with focal helical flow (432±162 ms vs. 195±82 ms, $p<0.001$). Reynolds numbers were between 1871 and 4037, and did not differ between CTL and pSSc (2978±654 vs. 2853±405, $p=0.509$). Inter-observer variability for the determination concerning the helical flow patterns was small, with κ strength of agreement of 0.867 (excellent agreement).

PA flow and WSS during one cardiac cycle

Table 2 shows the comparison of cine MRI parameters and PA flow features between CTL, entire pSSc, and pSSc without manifest PAH. WSS and OSI were visualized on 3D maps and quantified (Figure 2). There were no differences in LVEDVI, LVEF, SVI, RVEDVI, and RVEF between CTL and pSSc as well as pSSc without PAH. The PA area index was significantly greater in pSSc. The maximum area-averaged PA flow did not differ, whereas the minimum PA flow was significantly greater in pSSc. The overall WSS at the peak systolic phase (maximum WSS) was significantly lower (1.04±0.20 Pa vs. 1.33±0.34 Pa, $p<0.05$), whereas OSI (0.139±0.031, vs. 0.101±0.037, $p<0.01$) were greater in pSSc than in CTL. There were significant correlations between the PA area index and maximum WSS and OSI (Figure 3). Maximum WSS in subjects with focally or diffusely helical flow was significantly lower than in those with non-helical flow (focally helical: 1.00±0.10 Pa, diffusely helical: 1.05±0.22 Pa vs. non-helical: 1.39±0.31 Pa, respectively, $p<0.01$).

The relation between RV and PA

As shown in Figure 4A, PA acceleration time had a significant correlation with RVEF ($r=-0.47$, $p<0.01$). Significant correlation between PA pulatilitiy index and minimum flow in PA (Figure 4B. $r=-0.64$, $p<0.001$) was revealed, while no correlation was observed between PA pulsatility index and maximum flow in PA ($r=-0.48$, $p=0.80$). Finally, PA acceleration time and

RVSV/RVESV demonstrated significant negative correlation (Figure 4C. r=-0.46, p<0.01).

Outcome

All-cause death was detected in 4 pSSc of whom 2 patients were with manifest PAH. The cause of death included 1 with new PAH, 2 with lung cancer, 1 with colon perforation. MACE was observed in 4 pSSc, including 2 with acute myocardial infarction, 1 with new PAH (the same case as above), 1 with fatal arrhythmia. Eight pSSc hospitalized due to SSc or SSc-related comorbidity. The composite event of combined all-cause death and MACE were detected in 5 pSSc. As shown in Table 3, max WSS, min flow and Reynolds number were significantly lower in patients with the composite event. The ROC analysis to predict the composite event revealed statistical significance with the area under the curve (AUC) of 0.822 (p=0.031) with minimum flow in PA and the AUC of 0.933 (p=0.004) for Reynolds number whereas no significance with maximum WSS (p=0.053). The sensitivity and the specificity were 0.80 and 0.78 for minimum flow in PA (cut-off value, ≤9.22 ml/s) whereas 1.00 and 0.89 for Reynolds number (cut-off value, ≤2560). Cumulative event-free rate for the composite event were significantly lower in pSSc with minimum flow in main PA ≤9.22 ml/s (p=0.012, Figure 6A) and in pSSc with Reynolds number ≤2560 (p<0.001, Figure 6B).

Discussion

This is the report of the early changes of PA hemodynamics in pSSc using 4D-Flow. Visualization and quantification of cardiovascular hemodynamics may improve our understanding of normal and pathologically-altered cardiovascular physiology. A benefit of 4D-Flow compared to other imaging systems is the full 3D coverage of the great vessels and heart and the feasibility of retrospective analysis of flow at any location [13, 15].

In CTL, the non-helical flow continued during one cardiac cycle, but some showed focally helical flow during the late systolic and early diastolic phases. The helical flow was typically formed at the posterior wall of the main PA. The changes in distribution of flow velocity across the cross-section of the main PA might generate such a focally helical flow, which, however, did not spread to the whole PA branches [16]. The spatially heterogeneous WSS in the systolic phase may indicate the subsequent development of focally helical flow, especially in low WSS and high OSI areas.

Recent studies have shown that manifest PAH coincides with the appearance of helical flow in the PA and the early onset of retrograde flow with high sensitivity and specificity [16]. The relative period of helical flow correlated significantly with mean PA pressure [16]. Furthermore, continuous PA blood flow along the anterior PA wall after pulmonary valve closure was observed with manifest PAH, and this flow was accompanied by helical flow along

the posterior wall [16]. WSS in patients with PAH is reportedly decreased, which may reflect abnormal PA hemodynamics [10, 11]. When the vascular cross-sectional area increased, blood flow decreased and sometimes became rotational flow, resulting in decreased WSS [22]. In this study, only three pSSc had manifest PAH, but 11 without manifest PAH showed diffusely helical flow. Despite the comparable maximum area-averaged PA flow, the maximum WSS was significantly lower, whereas OSI were greater. These findings suggest that PA hemodynamics may already be altered in pSSc before clinical signs of manifest PAH become prominent. Comparing our results with a study by Barker et al. [23] in which patients with PAH included considerable number of SSc and demonstrated the slower blood flow and the lower WSS, the decreasing of maximum blood flow may explain the exacerbation of pulmonary vascular resistance and pressure.

WSS can be estimated in most of the vasculature by Poiseuille's law, which states that WSS is inversely proportional to the third power of the internal radius [24]. However, WSS in this study was obtained from the curve of the 3D velocity vector profile in vascular structures (supplementary Figure 1). Additionally, although both maximum WSS and OSI correlated with PA area index, the correlation coefficients were relatively low.

In pSSc, cellular infiltration and fibrotic changes in the PA wall have been reported [2, 3]. Furthermore, this study included patients with interstitial pneumonitis, low LVEF, and LGE in the LV wall. These complications might have chronically impaired RV function and prevented

a significant elevation of PA pressure [25]. However, since there was no difference in RVEF and RVEDVI between pSSc and CTL, the early change in the PA wall seems more likely to explain the altered PA flow without signs of manifest PAH. Notably, from the analysis of pressure-volume loops, Hsu et al. [21] reported a greater increase in RV volume during exercise in pSSc-related PAH than in those with idiopathic PAH, indicating depressed RV contractile reserve in pSSc.

Survival in SSc-related PAH is significantly worse than in idiopathic PAH [3, 5]. The altered PA flow may be a consequence of PA dilatation, but it also contributes to elevation of peripheral vascular resistance and PA wall stiffness by altering endothelial function and cellular extraction of inflammatory cytokines, forming a vicious cycle to manifest PAH [11, 26]. Considering this point, an earlier treatment with some vasodilators to improve aberrant WSS on the PA wall may decrease peripheral vascular resistance and then prevent the disease progression to manifest PAH. The 4D-Flow imaging is quite valuable to identify patients with altered PA flow at the stage before manifest PAH and to consider an earlier therapeutic approach. Although the composite outcome of all-cause death and MACE included non-PAH event such as lung cancer, acute myocardial infarction and fatal arrhythmia, they are suspected as following comorbidity of SSc [27, 28]. Considering the significant deterioration of WSS, PA flow and Reynolds number in the patients with composite events, the 4D-Flow characteristics may explain not only the hemodynamic abnormality but also the disease

progression of SSc.

The limitations are initially the small number of the subjects especially pSSc with manifest PAH. We performed no exercise testing for TTE which might result in the missing of exercise-induced PAH. The image of 4D-Flow is derived from the summation of cyclically repeating flow, thereby not expressing a real-time image. The low spatial and temporal resolution is also a limitation, and small or unstable blood flow may be missed. We selected a relatively high VENC setting for PA to enable additional assessment including aorta, which might miss small velocity changes. Very severe pSSc were excluded because they had other complications (e.g. renal dysfunction) or were generally too weak to tolerate long time scan. RV systolic pressure estimated by the simplified Bernoulli's equation has a limitation by ignoring the unsteady nature of the blood flow through the tricuspid valve [29]. Finally, most patients did not undergo right heart catheterization. However, it is not practical to perform invasive examinations for asymptomatic or less symptomatic patients without clinical signs of PAH.

In conclusion, different PA flow patterns and WSS between CTL and pSSc were demonstrated using 4D-Flow. In pSSc, 4D-Flow has a potential to detect the changes of PA hemodynamics in a non-invasive and comprehensive manner and to identify the patients at risk of PAH. These patients may benefit from the risk-stratified follow-up using 4D-Flow. Finally, 4D-Flow may also have a potential to predict adverse event in SSc. Further development of

4D-Flow technique may allow the physiological and pathological meanings of PA hemodynamics in pSSc to be elucidated.

Acknowledgment

Grant support

This study was supported by Ministry of Education, Science, Sports and Culture of Japan, Grants-in-Aid for Scientific Research (Grant Number 26461065 [HS]).

References

1. Hoeper MM, Bogaard HJ, Condliffe R, et al (2013) Definitions and diagnosis of pulmonary hypertension. *J Am Coll Cardiol*;62 **(**suppl 25):D42-D50.
2. Overbeek MJ, Mouchaers KT, Niessen HM, et al (2010) Characteristics of interstitial fibrosis and inflammatory cell infiltration in right ventricles of systemic sclerosis-associated pulmonary arterial hypertension. *Int J Rheumatol*;2010:604615.
3. Condliffe R, Howard LS (2015) Connective tissue disease-associated pulmonary arterial Hypertension. *F1000 Prime Reports*;7:06.
4. Hachulla E, Gressin V, Guillevin L, et al (2005) Early detection of pulmonary arterial hypertension in systemic sclerosis: A French nationwide prospective multicenter study. *Arthritis Rheum*;52:3792-800.
5. Lefevre G, Dauchet L, Hachulla E, et al (2013) Survival and prognostic factors in systemic sclerosis-associated pulmonary hypertension: A systematic review and meta-analysis. *Arthritis Rheum*;65:2412-23.
6. Rich JD, Rich S (2014) Clinical diagnosis of pulmonary hypertension. *Circulation*;130:1820-30.
7. Mukerjee D, St George D, Knight C, et al (2004) Echocardiography and pulmonary function as screening tests for pulmonary arterial hypertension in systemic sclerosis. *Rheumatology*;43:461-6.

8. Galie N, Rubin L, Hoeper M, et al (2008) Treatment of patients with mildly symptomatic pulmonary arterial hypertension with bosentan (early study): A double-blind, randomized controlled trial. *Lancet*;371:2093-100.

9. Coghlan JG, Denton CP, Grünig E, et al (2014) DETECT study group. Evidence-based detection of pulmonary arterial hypertension in systemic sclerosis: The DETECT study. *Ann Rheum Dis*;73:1340-9.

10. Tang BT, Pickard SS, Chan FP, Tsao PS, Taylor CA, Feinstein JA (2012) Wall shear stress is decreased in the pulmonary arteries of patients with pulmonary arterial hypertension: An image-based, computational fluid dynamics study. *Pulm Circ*;2:470-6.

11. Truong U, Fonseca B, Dunning J, et al (2013) Wall shear stress measured by phase contrast cardiovascular magnetic resonance in children and adolescents with pulmonary arterial hypertension. *J Cardiovasc Magn Reson*;15:81.

12. Mosbahi S, Mickaily-Huber E, Charbonnier D, et al (2014) Computational fluid dynamics of the right ventricular outflow tract and of the pulmonary artery: a bench model of flow dynamics. *Interact Cardiovasc Thorac Surg*;19:611-6.

13. Markl M, Kilner PJ, Ebbers T (2011) Comprehensive 4D velocity mapping of the heart and great vessels by cardiovascular magnetic resonance. *J Cardiovasc Magn Reson*;13:7.

14. Fluckiger JU, Goldberger JJ, Lee DC, et al (2013) Left atrial flow velocity distribution and flow coherence using four-dimensional flow MRI: A pilot study investigating the impact

of age and pre- and postintervention atrial fibrillation on atrial hemodynamics. *J Magn Reson Imaging*;38:580-7.

15. Föll D, Taeger S, Bode C, Jung B, Markl M (2013) Age, gender, blood pressure, and ventricular geometry influence normal 3D blood flow characteristics in the left heart. *Eur Heart J Cardiovasc Imaging*;14:366-73.
16. Reiter G, Reiter U, Kovacs G, et al (2008) Magnetic resonance–derived 3-dimensional blood flow patterns in the main pulmonary artery as a marker of pulmonary hypertension and a measure of elevated mean pulmonary arterial pressure. *Circ Cardiovasc Imaging*;1:23-30.
17. Takehara K, Satoh S. Kuwana M (2007) Guideline for the diagnosis of systemic sclerosis [in Japanese]. *The Japanese Ministry of Health and Welfare*:1-32.
18. Rudski LG, Lai WW, Afilalo J, et al (2010) Guidelines for the echocardiographic assessment of the right heart in adults: A report from the American Society of Echocardiography endorsed by the European Association of Echocardiography, a registered branch of the European Society of Cardiology, and the Canadian Society of Echocardiography. *J Am Soc Echocardiogr*;23:685-713.
19. Markl M, Chan FP, Alley MT, et al (2003) Time-resolved three-dimensional phase-contrast MRI. *J Magn Reson Imaging*;17:499-506.
20. Brau AC, Beatty PJ, Skare S, Bammer R (2008) Comparison of reconstruction accuracy

and efficiency among autocalibrating data-driven parallel imaging methods. *Magn Reson Med*;59:382-95.

21. Hsu S, Houston BA, Tampakakis E, et al (2016) Right ventricular functional reserve in pulmonary arterial hypertension. *Circulation*;133:2413-22.

22. Bürk J, Blanke P, Stankovic Z, et al (2012) Evaluation of 3D blood flow patterns and wall shear stress in the normal and dilated thoracic aorta using flow-sensitive 4D CMR. *J Cardiovasc Magn Reson*;14:84.

23. Barker AJ, Roldán-Alzate A, Entezari P, et al (2015) Four-dimensional flow assessment of pulmonary artery flow and wall shear stress in adult pulmonary arterial hypertension: results from two institutions. Magn Reson Med.;73:1904-13.

24. Malek AM, Alper SL, Izumo S (1999) Hemodynamic shear stress and its role in atherosclerosis. *JAMA*;282:2035-42.

25. Tedford RJ, Mudd JO, Girgis RE, et al (2013) Right ventricular dysfunction in systemic sclerosis-associated pulmonary arterial hypertension. *Circ Heart Fail*;6:953-63.

26. Li M, Stenmark KR, Shandas R, Tan W (2009) Effects of pathological flow on pulmonary artery endothelial production of vasoactive mediators and growth factors. *J Vascular Res*;46:561-71.

27. Katzen JB, Raparia K, Agrawal R, et al (2015). Early stage lung cancer detection in systemic sclerosis does not portend survival benefit: a cross sectional study. PloS one,

10(2), e0117829.

28. Butt SA, Jeppesen JL, Torp-Pedersen C, et al (2019) Cardiovascular Manifestations of Systemic Sclerosis: A Danish Nationwide Cohort Study. J Am Heart Assoc.;8(17):e013405.

29. Falahatpisheh A, Rickers C, Gabbert D, et al (2016) Simplified Bernoulli's method significantly underestimates pulmonary transvalvular pressure drop. *J Magn Reson Imaging*;43:1313-9.

Table 1. Clinical features in patients with SSc.

Number	23
Age (years old)	57.4±14.9
Sex (M/F)	2 / 21
Clinical PAH	3 (13.0%)
Disease duration (months)	77 (11.8-190.5)
Disease type (Limited/Diffuse)	10 / 13
NYHA (I/II/III/IV)	15 / 7 / 1 / 0
Serum NT-proBNP level (pg/ml)	91 (42.3-1052.0)
Systemic hypertension	9 (39.1%)
Interstitial pneumonitis	6 (26.1%)
Raynaud's phenomenon	20 (87.0%)
Medications	
Corticosteroids	11 (47.8%)
Immunosuppressants	5 (21.7%)
Calcium channel blockers	4 (17.4%)
ACEI/ARBs	8 (34.8%)
Prostanoids	7 (30.4%)
Phosphodiesterase-5 inhibitors	2 (8.7%)
Endothelin-1 receptor antagonist	1 (4.3%)
Autoimmune antibodies	
Anti-Scl-70 antibody	3 (13.0%)
Anti-centromere antibody	5 (21.7%)
Anti-U1-RNP antibody	7 (30.4%)

NT-proBNP: N-terminal-pro-brain natriuretic peptide, ACEI/ARBs: angiotensin converting enzyme inhibitors/angiotensin II receptor blockers, NYHA: New York Heart Association functional classes, PAH: pulmonary arterial hypertension. Data are number (%), mean±SD or medians with range.

Table 2. Comparison of parameters in cine MRI and PA flow.

	Control subjects	Patients with SSc (all)	Patients with SSc (without manifest PAH)
Number	10	23	20
Cine MRI			
LVEDVI (ml/m^2)	56.2±8.2	57.1± 13.5	59.0± 13.3
LVEF (%)	58.9±7.0	57.6±6.3	56.6±6.1
SVI (ml/m^2)	43.9±6.9	45.0±7.7	43.4±6.7
RVEDVI (ml/m^2)	65.9±15.7	66.3±15.0	64.0±12.6
RVEF (%)	62.2±7.9	62.0±9.6	62.1±9.3
Contrast-enhanced MRA			
PAAI (mm^2/m^2)	358.8±63.7	454.2±96.6**	446.6±84.1**
PA flow			
Max flow (ml/s)	224.5±51.4	235.8±28.2	237.9±28.3
Min flow (ml/s)	-2.7±18.9	7.7±16.0	10.5±12.5*
Max WSS (Pa)	1.33±0.34	1.04±0.20*	1.08±0.16*
Min WSS (Pa)	0.22±0.68	0.27±0.07	0.28±0.07*
OSI	0.101±0.037	0.139±0.031**	0.141±0.033**
Reynolds number	2978±654	2853±405	0.509

LVEDVI/RVEDVI; left/right ventricular end-diastolic volume index, LVEF/RVEF; LV/RV ejection fraction, Max/Min; maximum/minimum, OSI; oscillatory shear index, PAAI; pulmonary arterial area index, PAH; pulmonary arterial hypertension, SVI; stroke volume index, WSS; wall shear stress. Data are means±SD, *p<0.05, **p<0.01 vs. control subjects.

Table 3. Comparison of hemodynamic parameters between patients with or without composite event of all-cause death and major adverse cardiac event.

	Without events (n=18)	With events (n=5)	p
Max WSS (Pa)	1.08±0.17	0.85±0.20	0.021
OSI	0.143±0.033	0.123±0.017	0.208
Min flow (ml/s)	11.2±12.9	-5.1±20.9	0.039
Reynolds number	2989±336	2367±221	0.001

Max WSS; maximum wall shear stress, Min: minimum, OSI; oscillatory shear index

Figure legends

Figure 1. Streamline images of PA blood flow at peak systole, late systole, and early diastole and area-averaged main PA flow curves during one cardiac cycle

Cases are a control subject (A), patients with SSc with focally helical flow (**B**), with diffusely helical flow (**C**), and with manifest PAH (**D**). Arrows and * indicate helical flows and the analysis plane at main PA respectively. Subjects A to D are corresponding to supplementary movies 1 to 4. During systolic acceleration, the PA flow was non-helical, except for one patient with manifest PAH, and it increased from one cardiac phase to the next until reaching a maximum. The PA flow then decreased gradually until the pulmonary valve closed. The PA flow remained non-helical in the CTL at any phase (A), whereas it changed to helical flow (arrows) in pSSc (B-D). The helical flow was formed typically at the posterior wall of the main PA just below the right PA and was located in the main PA (B) or spread into the right and/or left PAs (C). In the patient with manifest PAH, the helical flow had already begun at the peak systolic phase and spread diffusely into the main, right, and left PAs (D).

Figure 2. Spatially heterogeneous WSS and OSI images at the PA wall

Left: WSS at the peak systolic phase and OSI images in a control subject (**A**, No. 3) and a patient with SSc (**B**, No. 18). Right: the changes in WSS of the whole PA wall during one

cardiac cycle. Representative images of WSS at the peak systolic phase were spatially heterogeneous both in the control (A) and the patient with SSc (B). The OSI images were also spatially heterogeneous (control: 0.002 to 0.491, SSc: 0.001 to 0.458), and the overall OSI was higher in the pSSc (control: 0.08, SSc: 0.15). In the pSSc, WSS and OSI seemed quite lower and higher, respectively, at the posterior wall (dorsal surface) compared with those at the anterior wall (visceral surface). The representative WSS curves at the entire PA walls had much lower maximum WSS in the pSSc (control: 1.80 Pa, SSc: 0.98 Pa).

Figure 3. Significant correlations between PA area index and maximum WSS **(A)** and OSI **(B)** The scattered data were obtained from both control subjects (white circles) and patients with SSc (black circles). The lines indicate regression lines and their confidence limits.

Figure 4. Significant correlations between RV-PA coupling parameters by 4D-Flow

The scattered data were obtained from both control subjects (white circles) and patients with SSc (black circles). The lines indicate the regression lines and their confidence limits.

Figure 5. The receiver-operating characteristics (ROC) for the prediction of the composite event by maximum wall shear stress (A), minimum flow in main PA (B), and Reynolds number (C)

The ROC analysis demonstrated no significance for maximum wall shear stress (A). In contrast, good accuracy for minimum flow in main PA (B) and excellent accuracy for Reynolds number (C) with statistical significance were observed.

Figure 6. Cumulative event-free rate for the composite outcome of all-cause death and major adverse cardiac events.

The event-free rates were significantly lower in the patients with minimum flow in main PA ≤9.22 ml/s ($p=0.012$, A) and in the patients with Reynolds number ≤2560 ($p<0.001$, B)

Supplementary Table 1. Clinical features and PA flow patterns.

Case #	Age	Sex	BSA (m^2)	HR (/min)	ECG abnorm-alities	TTE abnorm-alities	RVSP (mmHg)	EAE (mmHg/ml)	PAAI (cm^2/m^2)	LGE	Flow pattern	Location of helical flow	Origin of helical flow	Duration of helical flow (ms)	Reynolds number
Control															
1	56	M	1.71	81	-	-	N.A.	N.A.	2.54	-	NH	N.A.	N.A.	N.A.	3009
2	43	F	1.77	58	-	-	N.A.	N.A.	2.36	-	NH	N.A.	N.A.	N.A.	3199
3	30	F	1.6	57	-	-	N.A.	N.A.	3.65	-	NH	N.A.	N.A.	N.A.	4037
4	26	F	1.39	80	-	-	N.A.	N.A.	4.18	-	NH	N.A.	N.A.	N.A.	3605
5	53	F	1.39	87	-	-	N.A.	N.A.	3.99	-	FH	M	Post	134	2600
6	69	F	1.75	83	-	-	N.A.	N.A.	3.82	-	NH	N.A.	N.A.	N.A.	3148
7	78	F	1.37	58	-	-	N.A.	N.A.	4.11	-	FH	M	Post	158	2092
8	73	F	1.30	76	-	-	N.A.	N.A.	3.47	-	FH	M	Post	225	3295
9	60	F	1.58	70	-	-	N.A.	N.A.	3.77	-	FH	M	Post	145	3106
10	57	F	1.58	77	-	-	N.A.	N.A.	3.99	-	FH	M	Post	353	2742
SSc															
1	70	F	1.55	63	-	-	28	0.66	4.32	-	NH	N.A.	N.A.	N.A.	2502
2	56	F	1.54	65	-	-	19	0.35	4.45	-	NH	N.A.	N.A.	N.A.	2939
3	49	F	1.3	72	LAH	-	30	0.58	5.34	-	NH	N.A.	N.A.	N.A.	2589
4	17	F	1.42	79	-	Low LVEF	N.A.	N.A.	4.28	-	NH	N.A.	N.A.	N.A.	2381
5	71	F	1.38	83	AVB(I°)	-	23	0.43	4.68	RVin	FH	L	Post	190	3187
6	65	F	1.51	67	-	LAD, PE	N.A.	N.A.	3.61	-	FH	M	Post	92	2559
7	62	F	1.39	62	-	PE	25	0.39	5.54	-	FH	M	Post	185	3101
8	56	M	1.5	55	-	-	26	0.50	4.91	-	FH	M	Post	161	2966
9	31	F	1.56	92	-	-	N.A.	N.A.	5.14	MW	FH	M	Post	158	3057
10	77	F	1.43	64	-	-	33	0.58	5.5	-	DH	M/L	Post	507	3439
11	68	F	1.3	67	-	PE	25	0.36	4.39	-	DH	M/R	Post	201	3157

12	67	F	1.78	68	-	PE	37	0.64	2.88	-	DH	M/R	Post	221	2741
13	66	F	1.34	99	-	-	N.A.	N.A.	3.62	-	DH	M/L/R	Post	589	3609
14	57	F	1.5	64	-	-	21	0.44	4.54	-	DH	M/L/R	Post	210	2921
15	52	F	1.59	68	-	-	N.A.	N.A.	3	-	DH	M/L/R	Post	507	3159
16	52	F	1.43	73	-	-	N.A.	N.A.	5	-	DH	M/R	UD	221	3141
17	49	F	1.48	62	-	-	N.A.	N.A.	4.34	-	DH	M/L/R	Post	541	3293
18	47	F	1.59	57	-	-	25	0.51	5.75	-	DH	M/R	Post	492	2562
19	35	F	1.74	66	-	-	N.A.	N.A.	3.23	-	DH	M/R	Post	484	3125
20	70	F	1.42	54	-	-	32	0.42	4.79	-	DH	M/L/R	Post	427	2134
21	61	F	1.59	62	LVH	-	46	0.68	3.36	Dif	FH	M	Post	273	2616
22	64	F	1.49	45	TWA	LAD	44	0.42	6.87	RVin	DH	M/L/R	Post	575	2441
23	78	M	1.54	62	CRBBB	RVD	87	2.10	4.92	MW	DH	M/R	Post	651	2140

AVB; atrio-ventricular block, BSA; body surface area, CRBBB; complete right bundle branch block, Dif; diffuse infiltration, EAE; effective arterial elastance, ECG; electrocardiogram, HR; heart rate, LAD; left atrial dilatation, LAH; left anterior hemiblock, LVEF; left ventricular ejection fraction, LVH; LV hypertrophy, NH/FH/DH; non-helical/focally helical/diffusely helical flow, LGE; late gadolinium enhancement, M/L/R; main/left/right pulmonary artery, M/F; male/female, MW: mid-wall, N.A.; not available, PAAI; pulmonary artery area index, PE; pericardial effusion, Post; posterior wall, RVD; right ventricular dilatation, RVSP; RV systolic pressure, RVin; RV-insertion point, SSc; systemic sclerosis, TTE; trans-thoracic echocardiogram, TWA; T waves abnormality, UD; undetermined

Figure 1

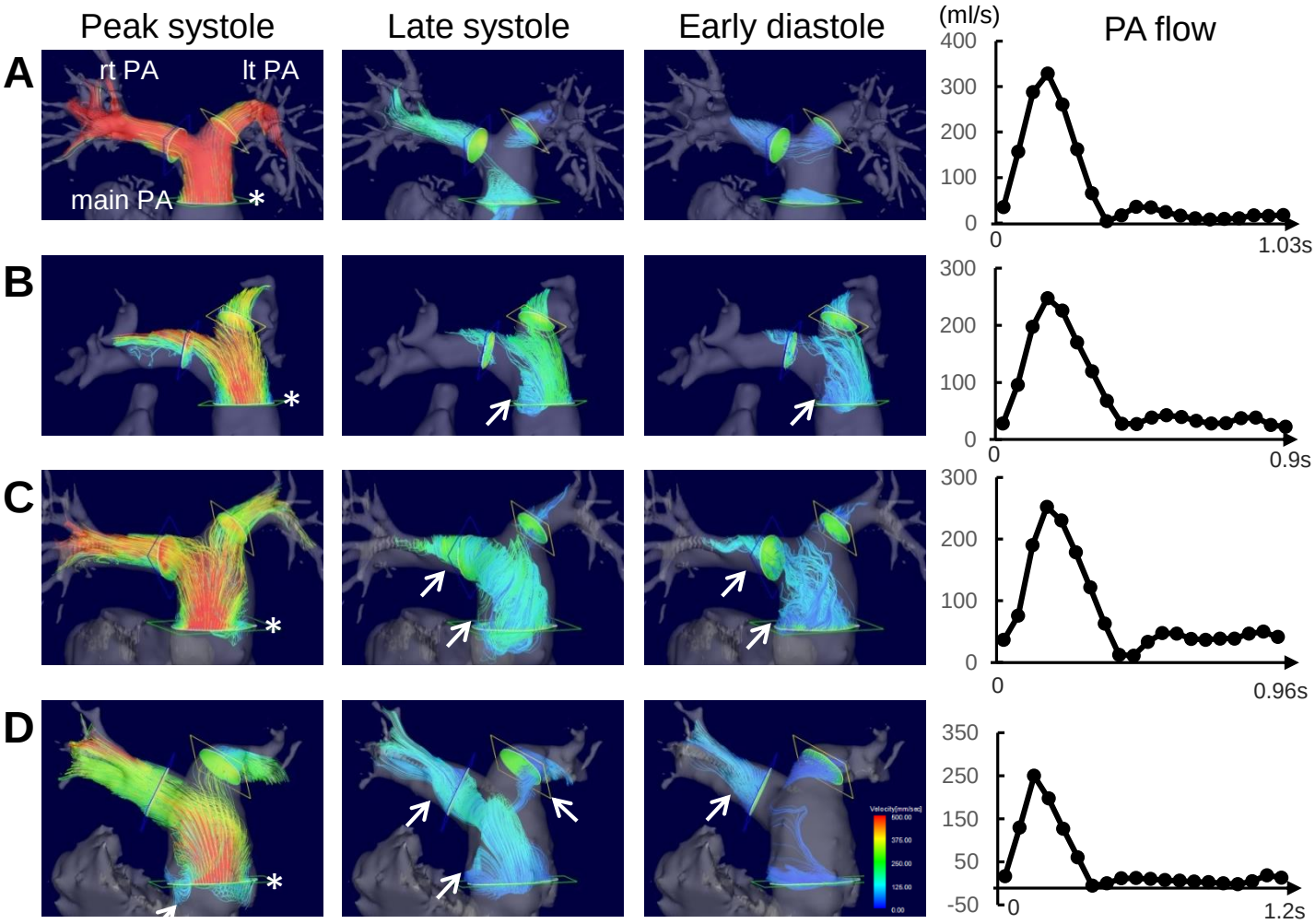
Peak systole
Late systole
Early diastole
PA flow
(ml/s)
A
rt PA
lt PA
main PA
*
400
300
200
100
0
0
1.03s
B
300
200
100
0
0
0.9s
C
300
200
100
0
0
0.96s
D
350
250
150
50
-50
0
1.2s

Figure 2

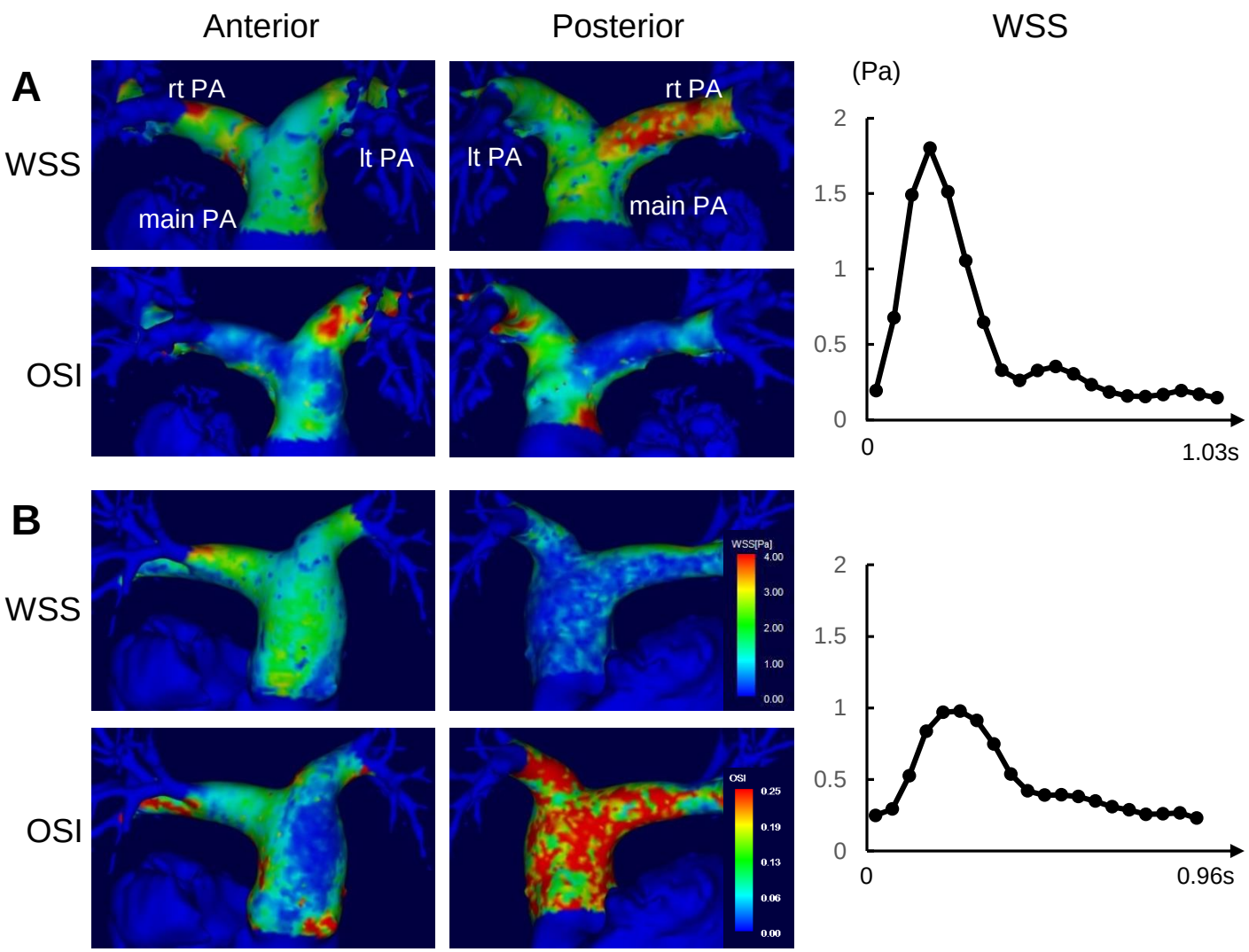
Anterior
Posterior
WSS
A
WSS
rt PA
lt PA
main PA
rt PA
lt PA
main PA
OSI
(Pa)
2
1.5
1
0.5
0
0
1.03s
B
WSS
WSS[Pa]
4.00
3.00
2.00
1.00
0.00
OSI
OSI
0.25
0.19
0.13
0.06
0.00
2
1.5
1
0.5
0
0
0.96s

Figure 3

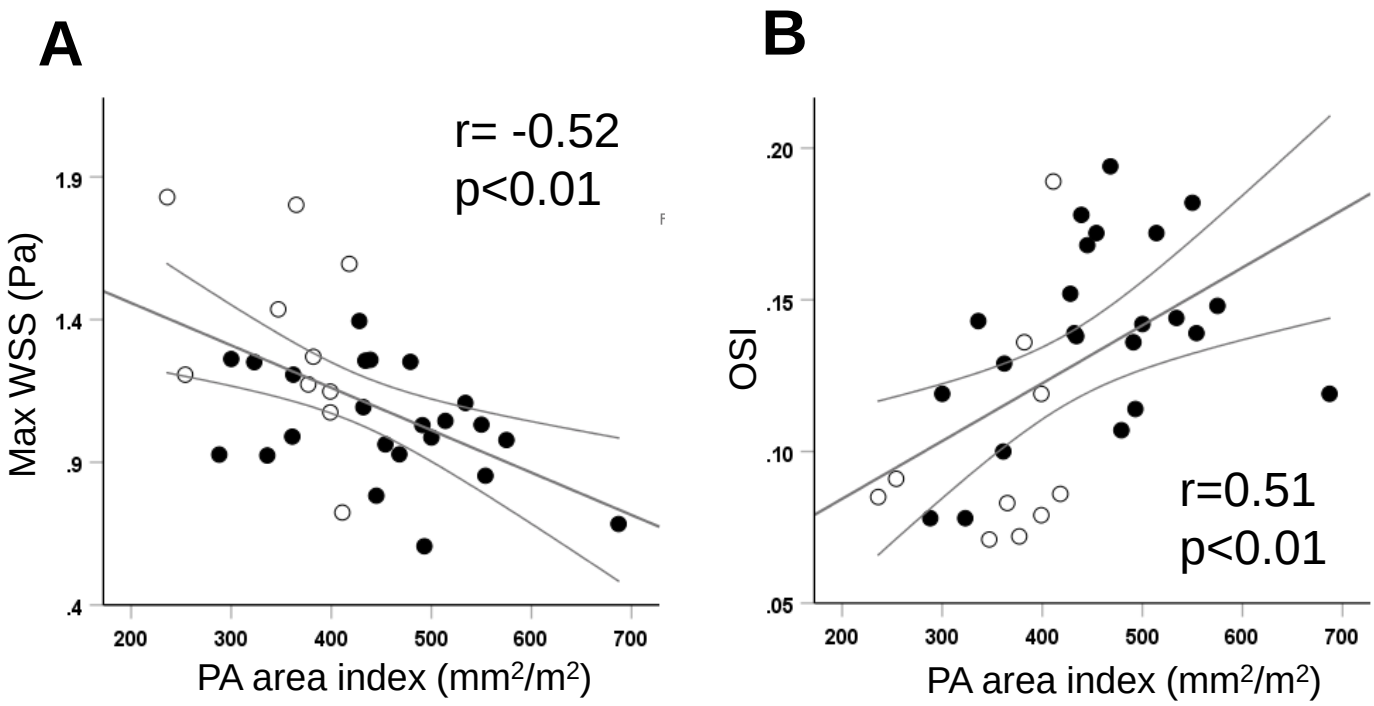
A
r= -0.52
p<0.01
Max WSS (Pa)
1.9
1.4
.9
.4
200
300
400
500
600
700
PA area index (mm2/m2)
B
OSI
.20
.15
.10
.05
r=0.51
p<0.01
PA area index (mm2/m2)

Figure 4

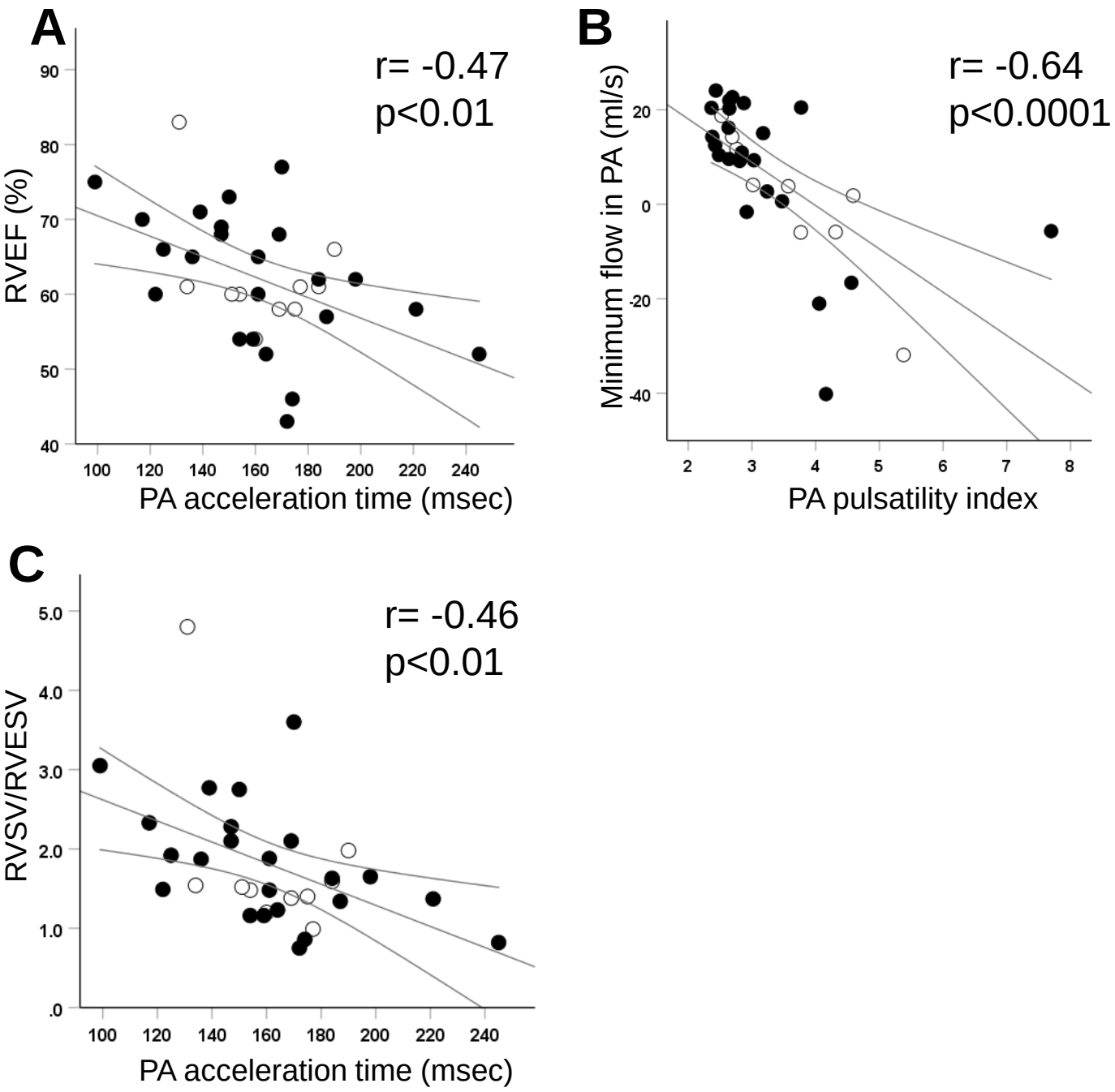
A
r= -0.47
p<0.01
RVEF (%)
PA acceleration time (msec)
B
r= -0.64
p<0.0001
Minimum flow in PA (ml/s)
PA pulsatility index
C
r= -0.46
p<0.01
RVSV/RVESV
PA acceleration time (msec)

Figure 5

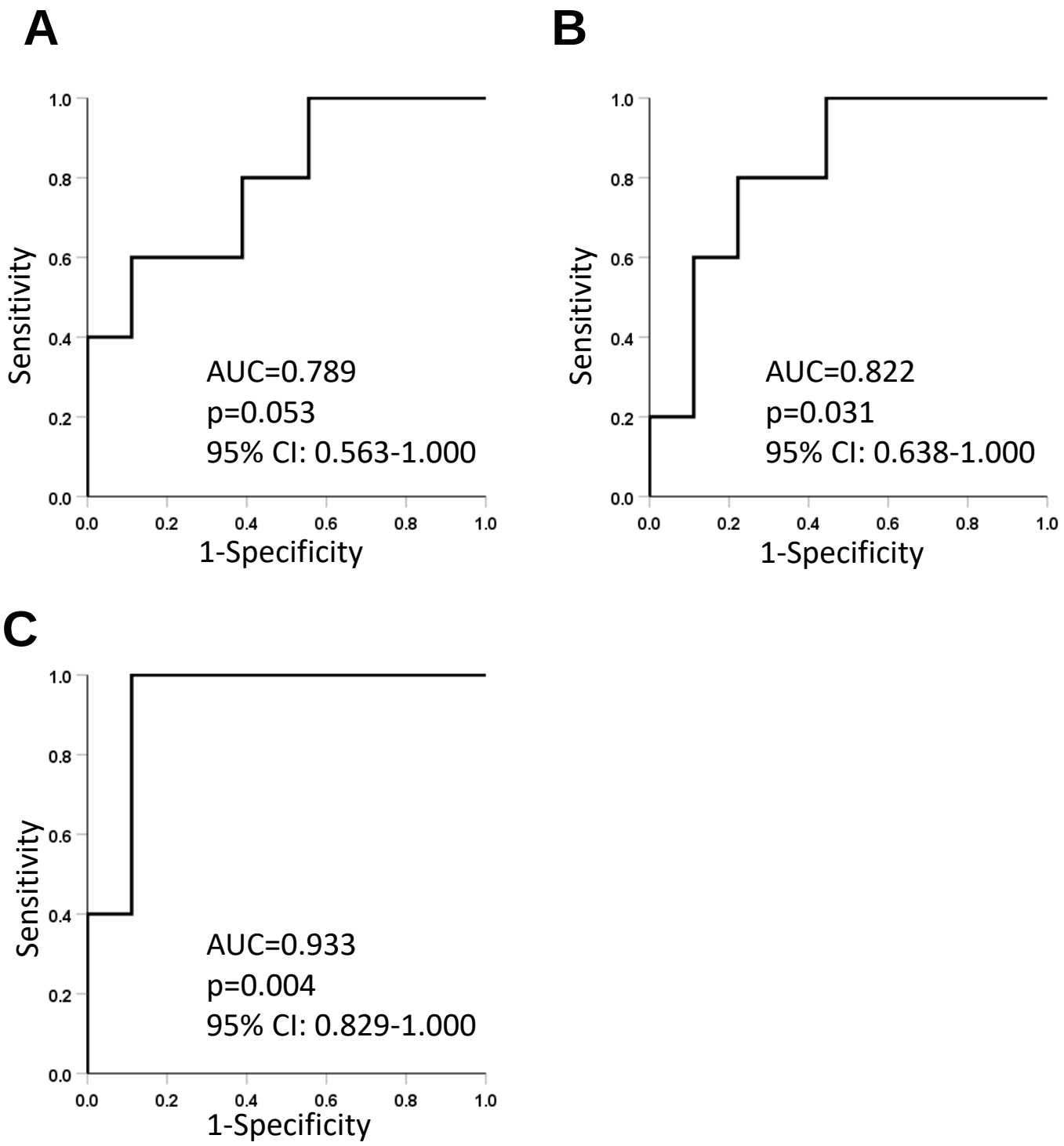
A
Sensitivity
1-Specificity
AUC=0.789
p=0.053
95% CI: 0.563-1.000
B
Sensitivity
1-Specificity
AUC=0.822
p=0.031
95% CI: 0.638-1.000
C
Sensitivity
1-Specificity
AUC=0.933
p=0.004
95% CI: 0.829-1.000

Figure 6

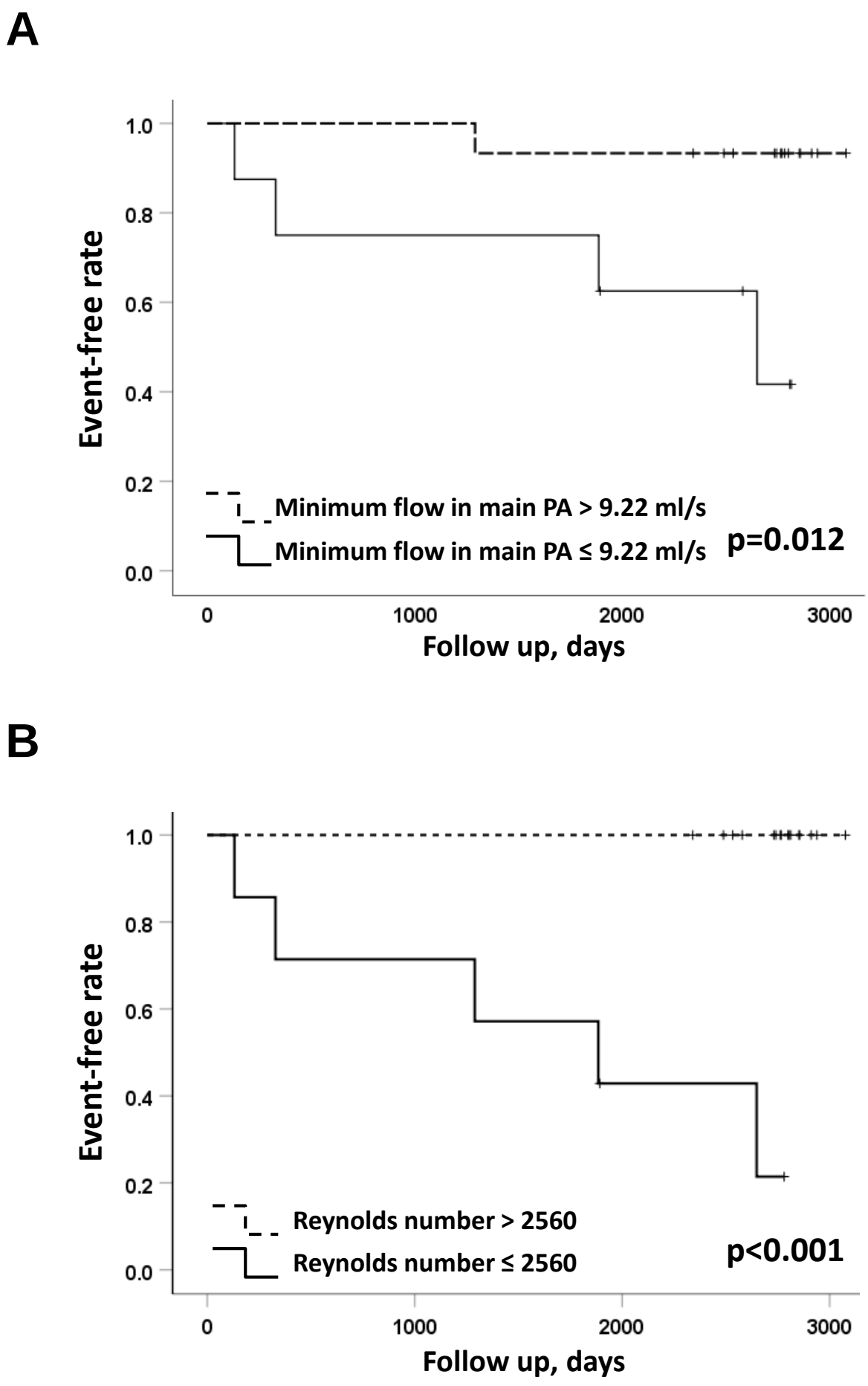
A
1.0
0.8
0.6
0.4
0.2
0.0
Event-free rate
Minimum flow in main PA > 9.22 ml/s
Minimum flow in main PA ≤ 9.22 ml/s
p=0.012
0
1000
2000
3000
Follow up, days
B
1.0
0.8
0.6
0.4
0.2
0.0
Event-free rate
Reynolds number > 2560
Reynolds number ≤ 2560
p<0.001
0
1000
2000
3000
Follow up, days